ACS APPLIED NANO MATERIALS

www.acsanm.org Article

# Effects of Graphitic and Pyridinic Nitrogen Defects on Transition Metal Nucleation and Nanoparticle Formation on N-Doped Carbon Supports: Implications for Catalysis

Vu T. Nguyen, Margaret A. Fitzgerald, Denali Ibbotson, Jayson Foster, Michael J. Dzara, Sarah F. Zaccarine, Shubham Vyas,* and Svitlana Pylypenko*

Cite This: *ACS Appl. Nano Mater.* 2022, 5, 14922−14933 Read Online

ACCESS | Metrics & More | Article Recommendations | Supporting Information

**ABSTRACT:** Functionalization of carbon supports with heteroatom dopants is now widely regarded as a promising route for stabilizing and strengthening the interactions between the support and metal catalysts. Tuning the type and density of heteroatom dopants allows for the tailoring of nanoscale catalyst−support interactions; however, an understanding of these phenomena has not yet been fully realized because of the complexity of the system. In this work, computational modeling, materials synthesis, and advanced nanomaterial characterization are used to systematically investigate the intriguing effect of the two most common nitrogen functionalities in the carbon-based supports on the interactions with selected transition metals toward realizing catalytic applications. Specifically, this study utilized density functional theory to evaluate adsorption energies and modes of adsorption for 12 metals located in groups 8−11 and periods 4−6 with pyridinic and graphitic N defects. Based on these results, further electronic structure investigation of the period 4 metals was conducted to elucidate periodic group trends. Experimental work included synthesis and nanomaterial characterization of a subset of materials featuring three metals each supported on two types of N-doped carbon supports and undoped graphene. Characterization of nanomaterials with scanning transmission electron microscopy and energy-dispersive X-ray spectroscopy confirmed that N functionalities enhanced the interactions with the selected transition metals when compared to the undoped support and demonstrated that the nature of the defect influences these interactions. Both computations and experiments agreed that Fe and Co are biased toward the graphitic sites over pyridinic sites, while Ni has an affinity to both defects without a statistically significant preference. This work established a correlation between computational and experimental work and a framework that can be expanded to other metals and alternative dopants beyond nitrogen in tailoring nanoscale catalyst−support interactions for a breadth of catalytic applications.

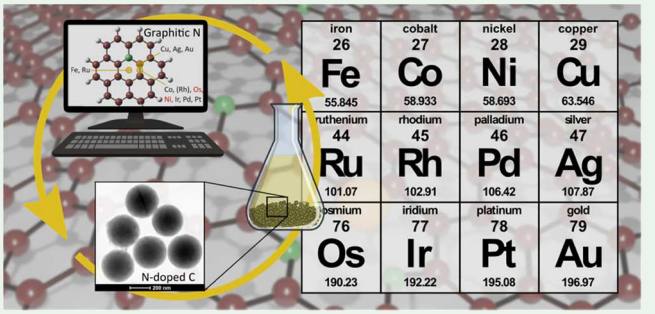


**KEYWORDS:** *N-doped, carbon supports, graphitic nitrogen, pyridinic nitrogen, adsorption energy, metal nucleation*



## 1. INTRODUCTION

Many applications that are at the core of technological advancement to combat the growing climate crisis at the nanoscale utilize supported metal catalysts to increase the reactive surface area of the catalyst and maximize the number of active sites. Metal in the supported catalysts can be dispersed on the support either in the form of metal nanoparticles (NPs), single atoms, or with metal atoms coordinated to support.[1,2] Most commonly, commercial carbons are used as the supports or matrix for many of these catalysts because of their accessibility and low cost, but the interactions between the metal NPs or single atoms and carbon can be weak, reducing the density of metal nucleation sites and, subsequently, catalytic active sites and limiting catalytic activity and durability.[3,4] Therefore, understanding and enhancing interactions between metal catalysts and their supports is critical to achieving increased performance and durability in supported catalyst systems.

It is not surprising that many research efforts have been dedicated to improving the understanding of the nanoscale metal−support interactions (MSIs), both for platinum group metal (PGM) and PGM-free catalysts in applications toward fuel cells, batteries, and gas storage[5−7] Carbons have good stability under harsh conditions, but it is well recognized that nucleation of metal nanoparticles on graphitized carbons is

**Received:** July 20, 2022
**Accepted:** September 2, 2022
**Published:** September 16, 2022

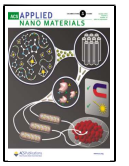




https://doi.org/10.1021/acsanm.2c03186
*ACS Appl. Nano Mater.* 2022, 5, 14922−14933

limited and localized predominantly at regions with defects, usually present on edges and between carbon support particles.[8] To increase the density of metal nucleation sites beyond these defects, researchers have studied the effects of changing the morphology and composition of the support.[9−12] A promising approach in catalyst−support enhancement is heteroatom doping of the carbon support with B, N, or S, which has been reported to improve the nucleation, catalytic activity, and stability of metal NPs due to the difference in electronegativity between the heteroatom and the support.[2,5,11,13−17] Of these heteroatom dopants, N has been most extensively studied, with demonstrations of improved nucleation, stability, and catalytic activity for both PGM and PGM-free catalysts.[7,16,18−21]

N concentration in carbon materials can be controlled to up to about 10 atomic percent, with fluctuations depending on the carbon material support.[13,22,23] Graphitic and pyridinic N are two of the most investigated types of N-dopants or defects, often displayed on graphene as an ideal theoretical model and workable material. It is acknowledged that pyrrolic N is another common N-dopant type that can be found alongside both graphitic and pyridinic N. However, pyrrolic N has a closer electronic structure to pyridinic N than both have with respect to graphitic N. In examining the literature for MSI in metal nucleation and stability, the existing gap has investigations lacking in a greater range of metals per defect type as many defect types have been investigated for more singular prominent metals, such as Pt. Computational studies have shown increased adsorption of Pt to graphene with pyridinic defects when compared to pristine graphene. These studies have also reported increased direct electronic interactions between Pt atoms with the pyridinic defects' N atoms.[11,17,24−28] It is experimentally demonstrated that pyridinic N aids in the nucleation and anchoring of catalyst NPs, with evidence of its presence improving the dispersion and stability of NP catalysts.[25,29−31]

Relative to the pyridinic defect, a graphitic defect is more thermally stable, given its chemical composition.[11,32] Thus, graphitic N speciation is more prevalent with N-doped supports synthesized with higher heat treatments, resulting in higher graphitic content. Typically, carbons with a very high graphitic content are desirable for improving corrosion resistance, but conversely, high graphitic content contributes to poor NP nucleation and catalytic dispersion. Several studies have demonstrated that a greater number of graphitic N is beneficial to Pt NPs' nucleation and dispersion due to the graphitic N's increased effect on the carbons' electron mobility, which has been linked to increased NP interactions and potential redox chemistries. In terms of dissolution, a theoretical study revealed that graphitic N improved resistance to dissolution in all cases for PtRu clusters while only presenting improvements with pyridinic N in select cases.[4]

A number of theoretical studies have directly compared the two defects, finding that Pt single atoms and nanoclusters had stabilizing effects with both defects.[11,24] While these studies explore the effects of pyridinic and graphitic N specifically for Pt, it is clear that the two defects may have different effects on other metals.[33] Both theoretical and experimental studies have shown that clusters of pyridinic nitrogen defects have been found to facilitate three-dimensional (3D)-transition metal (TM) interactions (most commonly Fe, Ni, and Co) through a metal−$N_4$ configuration; however, it was found that the same N configuration decreased the binding strength of heavier TMs such as Ir, Mo, Rh, and Ru.[34−36] Additionally, catalytic trends across transition metals with pyridinic defects have been examined, showing how different metals in a pyridinic environment are better tuned for certain electrochemical reactions.[37−42] In this manner, graphitic N defects have been explored to a lesser extent, but it has still been found that NPs nucleate around graphitic sites and have indirect interactions with the defects.[24,43] While informative, many studies focus primarily on the catalytic activity of different metals in an N-doped environment rather than the strength of the MSI. Additionally, some of these studies evaluate systems in which the metal is coordinated to N rather than dispersed on N-doped carbon support.

It is important to mention that experimental studies typically involve materials that have both types of these N defects in different amounts, and many other functionalities are also present. Theoretical studies are typically performed with one type of dopant, making it easier to compare the different defect types. The parameter space related to the potential beneficial effects of N-doping is still not explored in sufficient detail, requiring a deeper investigation into nitrogen concentration, type and relative amount of nitrogen functionalities, and catalyst composition. It is not practical to experimentally investigate the ideal N speciation for each TM that could have applications in catalysis. To address this gap in the literature, we present a detailed computational study of MSI for pyridinic and graphitic N, with a focus on TM nucleation, investigated as a function of metal electronic structure, and a set of computationally driven experimental syntheses that are used to verify computational results without requiring an impractically large number of nanoscale materials designed for catalytic support interactions.

To begin, theoretical studies scan 12 TMs, chosen for their relevancy in catalysis (Groups 8−11 and Periods 4−6), interacting with undoped graphene, a pyridinic N defect, and a graphitic N defect. MSI is presented as a function of valency for TMs to make direct comparisons of their electronic structure in the presence of these defects. Further calculations were performed on a downselected set of metals including Fe, Co, Ni, and Cu to better understand the specific electronic changes seen in the metals when interacting with the three different support materials. To validate and compare computational results, pyridinic- and graphitic-rich N-doped carbon (NC) materials were synthesized and analyzed using X-ray photoelectron spectroscopy (XPS) to confirm chemical speciation. These two types of NC supports along with undoped graphene were then physically mixed with metal precursors of each of the four metals from the computational study and pyrolyzed to reduce the metal on each support. The extent of metal incorporation on the transition metal nitrogen-doped carbons (TM-NCs) was determined using scanning transmission electron microscopy (STEM) paired with energy-dispersive X-ray spectroscopy (EDS) and subsequently correlated with results from the computational study.

## 2. METHODS

**2.1. Theoretical Methods.** The Gaussian16 software package was implemented for density functional theory (DFT) calculations using the hybrid Perdew−Burke−Ernzerhof (PBE1PBE) functional with 6-31+G(d) basis sets for nonmetal atoms and def2-TZVPD for metal atoms, alongside previously reported values.[44,45] Truncated carbon support models containing 24 carbon atoms were utilized, in which further details about their design modeling choices and parametric


https://doi.org/10.1021/acsanm.2c03186
ACS Appl. Nano Mater. 2022, 5, 14922−14933

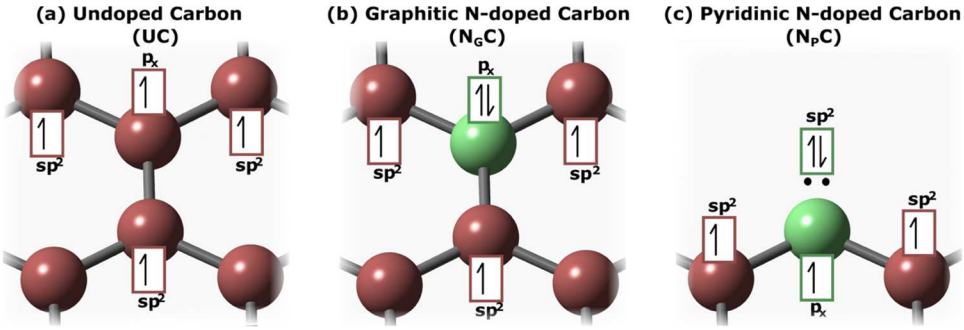


**Figure 1.** (Bottom): the electron allocation from the carbon atom and the replacement nitrogen atom through graphitic and pyridinic defects are shown where the electrons originating from those atoms are depicted on the support. Each individual electron and its spin are shown as an arrow. The corresponding text presents the [hybridized] orbitals of those atoms that the electrons are allocated to, and the two dots represent a lone pair for the following substrates: (a) undoped carbon, (b) graphitic N-doped carbon, and (c) pyridinic N-doped carbon.

considerations, including the model size truncation choice, have been investigated and discussed in a previous study involving comparisons to other studies in the literature that have employed such models.[44] Similarly, optimizations of the metal with the carbon support were carried out from four positions for the graphitic- and pyridinic-containing models, whereas the undoped had three.

Counterpoise corrections were used to account for basis set superposition error.

$$E_{ads} = E_{MS} - E_M - E_S \quad (1)$$

The adsorption energy ($E_{ads}$) was calculated using eq 1. Here, $E_{ads}$ is the counterpoise corrected adsorption energy, $E_{MS}$ is the energy of the metal−support complex, and $E_M$ and $E_S$ are the energies of the metal and support, respectively, corrected through counterpoise. $E_{ads}$ is discussed in a manner where increases refer to the increases in magnitude/strength rather than the absolute values (and vice versa).

**2.2. Experimental Methods.** *2.2.1. Synthesis of NC Nanomaterials.* N-doped carbon spheres were synthesized following a modified solvothermal synthesis reported by Wickramaratne et al.,[46] which we have previously detailed in a recent publication.[47] A solution of 640 mL of deionized $H_2O$ (18.2 M·Ω) and 256 mL of ethanol (Pharmco-Aaper, 200 proof absolute anhydrous) was prepared and stirred at 300 rpm. Then, 6.4 g of resorcinol (Sigma-Aldrich, >99%) was added to the solution and stirred until dissolved. Using a cannula and nitrogen gas, 10.8 mL of ethylenediamine (Sigma-Aldrich, >99.5%) was transferred from its septum-sealed container and added to the aqueous alcohol solution. Lastly, 9.6 mL of formaldehyde (Alfa Aesar, 37 wt %) was added to the solution, which was then stirred continuously for 24 h at room temperature. The solution was then solvothermally treated by sealing the screw-top 2 L high-density polyethylene bottle with DuraFilm and heating at 100 °C for 24 h. Once cooled, polymerized spheres were centrifuged at 8750 rpm in a Marathon 22 KBR centrifuge for 15 min, where the excess solution was aspirated, and then the remaining product was dispersed in ethanol and air-dried at 70 °C for 12 h to remove the ethanol. The dried polymer spheres were pulverized into a fine powder via a mortar and pestle and pyrolyzed in a quartz boat at variable temperatures under $N_2$ flowing at 100 sccm. The pyrolysis heating curve included an initial slow ramp of 2 °C/min to 350 °C, a 4 h dwell at 350 °C, and then a final ramp of 5 °C/min to either 600 (for 600 NC) or 900 °C (for 900 NC), where it dwelled for 2 h before cooling to room temperature.

*2.2.2. Synthesis of TM-NC Nanomaterials.* TM-NCs were synthesized by depositing metal-containing precursors onto NC material. The following precursors were used to make TM-NCs: Fe, 24.7 mg of $FeCl_2$; Ni, 25.2 mg of $NiCl_2$; Co, 26.0 mg of $CoCl_2$; and Cu, 12.5 mg of $CuCl_2$ (Sigma-Aldrich). First, TM-chloride precursors were dissolved in 100 mL of methanol Pharmco-Aaper (200 proof absolute anhydrous). Once the TM-chloride was dissolved, 100 g of the respective carbon support (Sigma-Aldrich Graphene nano-Platelets 300 (GNP) (CAS# 7782-42-5), 600 NC, or 900 NC) was added to the methanol−TM solution and physically mixed using a kitchen-style hand mixer for 10 min. Then, this "kitchen-style" mixing continued for an additional 10 min while in a sonicating bath. The beakers with the mixture were then heated in a furnace at 70 °C for 24 h to remove methanol. The resulting product was then pyrolyzed under $N_2$ flowing at 100 sccm using a simple heating curve that ramped at 10 °C/min to the desired heat treatment temperature (400, 600, or 800 °C), dwelled for 4 h, and cooled to room temperature.

*2.2.3. Scanning Transmission Electron Microscopy/Energy-Dispersive X-ray Spectroscopy.* All samples for STEM/EDS analysis were prepared using a dry application method on Cu grids, except for the Cu samples that were prepared on Au TEM grids. Micrographs were obtained using an FEI Talos F200X instrument at 120 kV accelerating voltage to increase the EDS counts of these materials, which have low $Z$ values. Elemental maps were collected for each sample in at least five different locations for at least 5 min. Quantification for each sample was obtained using identical EDS quantification procedures provided in the Bruker EDS analysis program.

*2.2.4. X-ray Photoelectron Spectroscopy.* XPS measurements were performed using a custom Scienta-Omicron HiPP-3 system equipped with an R4000 hemispherical analyzer operating in a swift acceleration mode, calibrated to the Au 4f region (83.95 eV) of a sputter-cleaned Au foil. A focused Al K$\alpha$ X-ray source (1486.6 eV) was operated with a 900 $\mu$m spot size at 300 W. The X-ray beam was incident normal to the sample. NC powder samples were mounted onto double-sided conductive carbon tape. Survey and high-resolution spectra (C 1s, N 1s, O 1s) were acquired at pass energies of 50 eV. A 0.8 mm × 30 mm slit size was used, resulting in an estimated energy resolution of approximately 0.59 eV. The analysis chamber was maintained at a level below $5.0 \times 10^{-8}$ mbar, while the analyzer pressure remained below $5.0 \times 10^{-9}$ mbar. Three unique spots on each sample were used to measure the high-resolution spectra. The spectra from each of the three unique areas were then summed, improving both the signal-to-noise ratio and spatial averaging. An additional spot on each sample was used to acquire the survey spectrum.

## 3. RESULTS AND DISCUSSION

**3.1. MOA and $E_{ads}$ of 12 TM on Undoped and N-Doped Carbon Supports with Graphitic and Pyridinic Defects.** Theoretical studies began with designing a truncated representation of a graphene surface, as portrayed with the "two-shell" model, to represent the simplest forms of graphitic and pyridinic defects from nitrogen doping. Figure 1 provides the key differences in electronic structures of the supports defined by their defects [or lack thereof]. The electronic distribution of the electrons from the nitrogen atom of the defects or the carbon atom that is replaced by the defects is presented for the following substrates: undoped carbon (UC), N-doped carbon with a graphitic defect (N$_G$C), and N-doped


https://doi.org/10.1021/acsanm.2c03186
ACS Appl. Nano Mater. 2022, 5, 14922−14933

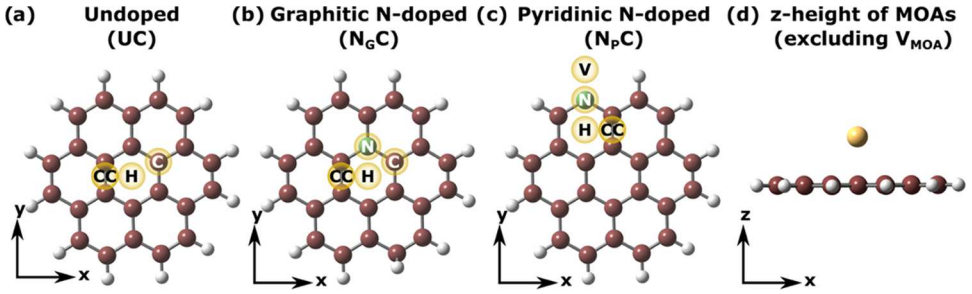


**Figure 2.** Annotated starting locations for the metal atom over the carbon-surface models containing no defect (a), graphitic defect (b), or pyridinic defect (c). The letter labels denote these locations (each model is not all-inclusive of every location): over the hole directly between the surrounding carbon atoms and the nitrogen atom ($H_{MOA}$), over the nitrogen of the graphitic defect and its adjacent bonds ($N_{MOA}$), over the inner carbon atom adjacent to the nitrogen ($C_{MOA}$), over the inner carbon−carbon bond adjacent to the nitrogen−carbon bond ($CC_{MOA}$), and in-plane with the carbon surface next to the nitrogen of the pyridinic defect ($V_{MOA}$). All locations, except for $V_{MOA}$, are directly above the carbon model exemplified in (d).

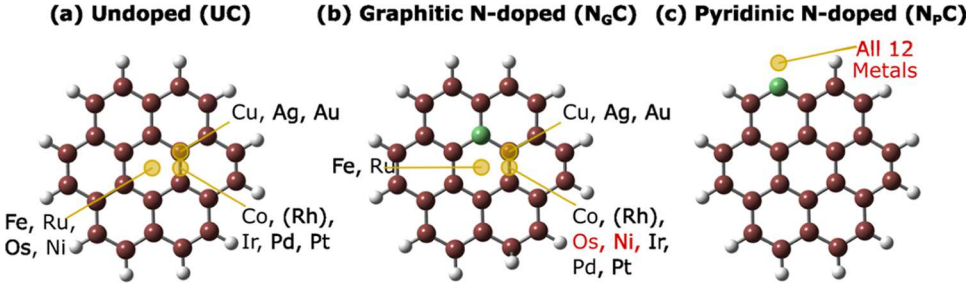


**Figure 3.** Graphically depicted MOA of the 12 metals on the supports from Table 1 labeled (a) undoped carbon, (b) graphitic N-doped carbon, and (c) pyridinic N-doped carbon. The red font represents that the metal changed its MOA from the undoped to the doped supports, and Rh in parentheses represents that the metal relaxed to an edge version of the MOA.

carbon with a pyridinic defect ($N_PC$). $N_GC$ simply introduces one more electron as compared to the carbon it replaces in UC. The other electronic components are the same as those of UC as it forms three $\sigma$-bonds with the adjacent carbons, and the fourth electron resides in its $p_z$ orbital to participate in the $\pi$-network. The additional fifth electron is then promoted to the conduction band. On the other hand, the electronic structure of $N_PC$ is entirely different. The nitrogen forms two $\sigma$ bonds with adjacent carbons and donates the third electron to the $\pi$-cloud, leaving a filled $sp^2$ orbital available to the metal.

Figure 2 defines the mode of adsorption (MOA) positions where the metal is located when introduced to each of the studied supports. The MOA positions are defined as over the C−C bond ($CC_{MOA}$), over the "hole" or center of the carbon ring ($H_{MOA}$), directly over a carbon atom ($C_{MOA}$), directly over the N atom ($N_{MOA}$), and in the plane of the graphene at a vacancy ($V_{MOA}$, only in $N_PC$). The specific locations for each support are visualized in Figure 2, along with a side profile showcasing the vertical height of each MOA with regard to the graphene (applies to all but the $V_{MOA}$). The effect of edge sites has been considered and explored in a previous publication.[44]

This study evaluated the most favorable MOA interactions between 12 TMs (Fe, Co, Ni, Cu, Ru, Rh, Pd, Ag, Os, Ir, Pt, Au) and their support by determining the location with the greatest adsorption strength ($E_{ads}$) on each of the carbon supports. All $E_{ads}$ and MOA calculations are presented in Table S1 for reference. It is important to note that Ru was not fully optimized, which has been factored into the following results and discussion. Figure 3 presents the observed MOAs for all TMs over the UC, $N_GC$, and $N_PC$ supports. $N_PC$ and $N_GC$ appear to affect the MOA for all metals in a manner that is defect-dependent compared to UC. For $N_GC$, none of the MOA directly interact with the graphitic nitrogen atom as the electronic structure defined by UC is still largely present with a slightly greater electronic density due to the additional N electron. This is supported by the fact that most TMs maintain the same MOA as was observed with UC, with the exceptions highlighted in Figure 3.

Interestingly, Os attained a $CC_{MOA}$ compared to its group's $H_{MOA}$ when it interacted with $N_GC$, which may be due to the combination of the size difference compared to Fe and slight deviations in orbital fulfillment, energies, and geometries when compared to Ru. The 6s orbital of Os gains electronic occupancy with a graphitic N, whereas there is a less relative change in Ru's valance orbitals.[44] It is possible then that the 6s orbital size hinders its ability to fit into the $H_{MOA}$ and shifts to the $CC_{MOA}$, where it has greater $E_{ads}$. In the case of Ni on UC, it favored the $H_{MOA}$ while its group was positioned at the $CC_{MOA}$. Similarly, the increased electronic density from graphitic defect in the $CC_{MOA}$ location places the HOMO from the d-orbitals to the valence 4s orbital (Figure S1). In doing so, it reduces Ni's stabilization over the $H_{MOA}$ and favors the $CC_{MOA}$, such as Pd and Pt. Ni's differential MOA on UC is suspected to be due to its smaller size compared to its group members. In combination with its smaller size, it can electronically be better stabilized over the $H_{MOA}$ than if it were to have energetically higher occupied orbitals such as those in Pd and Pt.

When introduced to the $N_PC$ support, all TMs situate themselves in the $V_{MOA}$ (Figure 2). This $V_{MOA}$ of the TM aligns with the in-plane $sp^2$ orbital as opposed to the other MOAs that sit over the carbon plane as these TMs are electrophilic and attracted to the sterically favorable $sp^2$ electronic density. To summarize, $N_GC$ largely does not


https://doi.org/10.1021/acsanm.2c03186
ACS Appl. Nano Mater. 2022, 5, 14922−14933

change the MOA for the supported TM, while $N_PC$ adjusts all of the MOA to the $V_{MOA}$. This indicates that the $N_GC$ enhances the existing MSI while $N_PC$ introduces a new enhanced MSI altogether.

The calculated $E_{ads}$ provides a quantitative metric of MSI for each metal, with a more negative value representing greater adsorption (Table 1). To clarify this convention, note that in this work, an "increase" in $E_{ads}$ denotes a greater absolute value and therefore a stronger interaction with the support and vice versa. Table 1 demonstrates that almost all metals show an increase in $E_{ads}$ with both types of defects, except for Ru, Rh, and Ir, which decrease with $N_PC$.

**Table 1. Greatest $E_{ads}$ (More Negative Implies Greater MSI as Formerly Presented) of the 12 Metals Supported on the Three Carbon Models**

| | | $E_{ads}$ | | |
|---|---|---|---|---|
| group | name | undoped | graphitic | pyridinic |
| group 8 | Fe | −1.58 | −1.85 | −1.70 |
| | Ru | −2.67 | −4.61 | −2.14 |
| | Os | −2.54 | −3.42 | −2.68 |
| group 9 | Co | −0.06 | −1.89 | −0.57 |
| | Rh | −2.17 | −2.26 | −1.20 |
| | Ir | −1.36 | −3.79 | −0.83 |
| group 10 | Ni | −1.78 | −2.44 | −2.37 |
| | Pd | −0.82 | −1.36 | −0.92 |
| | Pt | −1.79 | −3.05 | −2.22 |
| group 11 | Cu | −0.02 | −0.19 | −0.45 |
| | Ag | −0.02 | −0.05 | −0.20 |
| | Au | −0.04 | −0.52 | −0.42 |

In Group 8, which includes Fe, Ru, and Os, $E_{ads}$ on UC is the lowest for Fe with −1.58 eV, while Ru and Os have higher $E_{ads}$ of −2.67 and −2.54 eV, respectively. With $N_GC$, all $E_{ads}$ increase; Fe increases by 0.23 eV, Ru by 1.94 eV, and Os by 0.88 eV. The introduction of a pyridinic N in $N_PC$ results in an increase of 0.12 and 0.14 eV with Fe and Os, respectively, but a decrease of 0.43 eV for Ru. The $E_{ads}$ for Ru on $N_PC$ may be flawed given its failed optimization due to its flat potential energy surface in the $V_{MOA}$. With this consideration, the $E_{ads}$ results support that either defect increases the adsorption strength in Group 8, with a slight $E_{ads}$ bias toward $N_GC$ over $N_PC$.

The Group 9 elements Co and Ir show a larger $E_{ads}$ increase when comparing UC to $N_GC$ whereas $E_{ads}$ for Rh only increases slightly. The presence of a graphitic N increases Co $E_{ads}$ by 1.83 eV, Rh by 0.09 eV, and Ir by 2.43 eV. The increase of $E_{ads}$ for $N_PC$ is much less, with 0.51 eV for Co, while Rh and Ir decrease their $E_{ads}$ with the $N_PC$ support compared to UC. Group 10 of Ni, Pd, and Pt show the greatest increase in $E_{ads}$ across all of the group metals for both defects. In $N_GC$, Ni, Pd, and Pt increase their $E_{ads}$ by 0.66, 0.54, and 1.26 eV, respectively. In $N_PC$, Ni, Pd, and Pt increase their $E_{ads}$ by 0.59, 0.10, and 0.43, respectively.

Group 9 presents the most apparent $N_GC$ bias of all groups, as the increase of $E_{ads}$ for Co and Ir is much larger with $N_GC$ than $N_PC$. The $E_{ads}$ with the $N_PC$ for these metals further supports this bias since there was very little $E_{ads}$ increase in Co, and the $E_{ads}$ actually decreased for Rh and Ir (Ru was the only other metal outside of this group that presented an $E_{ads}$ decrease, which could be attributed to the failed optimization). Co does then slightly stand out from the other group members as its $E_{ads}$ increases rather than decreases. With its atomic size being a distinguishing factor from Rh and Ir, Co is more easily polarized by the pyridinic N's lone pair, contributing to the slightly enhanced $E_{ads}$. In $N_GC$, Co is positioned over the support versus in $N_PC$ where it is in the same basal plane, increasing the possible orbital overlap and further improving $E_{ads}$. More electronic density is located over the surface from graphitic defects than pyridinic defect's lone pair in the basal plane, potentially explaining the bias toward $N_GC$ for Co. On comparing this group with the other studied metals, the drastic difference in $E_{ads}$ of $N_GC$ and $N_PC$ implies a greater defect preference.

The smallest change was seen for Group 11 metals where Cu, Ag, and Au show minimal $E_{ads}$ (∼0 eV) with UC. For Cu and Ag, the $E_{ads}$ only slightly increases, favoring $N_PC$ over $N_GC$, albeit both dopants increase $E_{ads}$ to a much smaller extent than the rest of the metals presented in this work. Only Au has a larger than 0.4 eV increase from N-doping within Group 11, demonstrating similar values for both defects. While N-doping Group 11 may show some adsorption changes at an initial glance, the absolute $E_{ads}$ values are much lower compared to the other groups. It should also be noted that only the Group 11 TMs locate themselves on the $C_{MOA}$, as they are only capable of interacting with one carbon atom (if at all), and thus, this $C_{MOA}$ implies low-strength MSI.

Through the evaluation of MOA and $E_{ads}$ of the 12 TMs, it was observed that the two presented defects are distinctly electronically different. This reinforces that there is a sense of tunability for the MSI in the selection between $N_GC$ and $N_PC$ shown through the MOA. This tunability is extended as some periodic metal groups have a unique preferential adsorption bias that can be preferentially tuned with respect to other metal groups. Group 11 presents a slight bias toward $N_PC$; however, the MSIs appear to be minimal despite this. Group 10 demonstrates improvements in MSI for both defects, with some extent of $N_GC$ preference. Lastly, Groups 8 and 9 are the most evident in their adsorption bias toward $N_GC$.

**3.2. Electronic Structure Analysis of Fe, Co, Ni, and Cu.** Based on the results of initial computations, Fe, Co, Ni, and Cu were selected for deeper electronic analysis, including partial atomic charge and electronic densities, to further evaluate the fundamental chemistries of the MSI in whether it is charge transfer-based or some form of chemical/electronic rearrangement.[48,49] Since group members typically behave similarly, the selected metals from each group act as valid predictors for the behavior of their respective elements in lower periods; the comparison of metals from the same period is also more insightful. These leading group members present the defect bias held by their respective groups.

Table 2 shows the charges on the four metals. For all metals, the difference in partial charge from UC to $N_PC$ is greater than from UC to $N_GC$. It is conceded that these charges are relatively neutral, but defect-specific trends are presented, where the difference is more pronounced with Fe and Ni compared to Co and Cu. This again supports that the nature of the MSI changes with $N_PC$ as compared to UC and $N_GC$ and to a greater extent with Fe and Ni. Co and Cu may not lose as much electronic density due to their unpaired electron. It could be assessed that the charge differences are not significant enough to claim charge transfer for these specific MSIs; however, some degree of electronic density change with the $N_PC$ is evident. Table 3 presents an electronic description of the metals over UC, $N_GC$, and $N_PC$ (along with its atomic


https://doi.org/10.1021/acsanm.2c03186
ACS Appl. Nano Mater. 2022, 5, 14922−14933

**Table 2. Comparison of the Four Downselected Metals with the Undoped and Doped Carbon Supports and Their Partial Charge (q)**

| | | q |
|---|---|---|
| Fe | undoped | 0.41 |
| | graphitic | 0.42 |
| | pyridinic | −0.08 |
| Co | undoped | 0.10 |
| | graphitic | 0.12 |
| | pyridinic | 0.05 |
| Ni | undoped | 0.40 |
| | graphitic | 0.28 |
| | pyridinic | −0.01 |
| Cu | undoped | −0.01 |
| | graphitic | 0.01 |
| | pyridinic | −0.05 |

**Table 3. NBO Analysis of the Valence Orbitals of the Four Metals across the Three Supports and in Their Atomic Form**

| | | orbital occupation analysis | | | | | |
|---|---|---|---|---|---|---|---|
| metal | environment | s | $d_{xy}$ | $d_{xz}$ | $d_{yz}$ | $d_{x^2-y^2}$ | $d_{z^2}$ |
| Fe | atomic | 1.50 | 2.00 | 2.00 | 2.00 | 0.00 | 0.49 |
| | undoped | 0.05 | 1.72 | 1.81 | 0.24 | 1.65 | 1.97 |
| | graphitic | 0.06 | 1.52 | 1.33 | 1.03 | 1.56 | 1.96 |
| | pyridinic | 1.29 | 1.92 | 1.82 | 0.03 | 1.23 | 1.75 |
| Co | atomic | 1.00 | 2.00 | 2.00 | 2.00 | 1.00 | 1.00 |
| | undoped | 0.97 | 1.99 | 1.68 | 1.97 | 1.03 | 1.15 |
| | graphitic | 0.99 | 1.17 | 1.82 | 1.65 | 1.88 | 1.28 |
| | pyridinic | 0.97 | 1.79 | 1.88 | 1.99 | 1.21 | 1.00 |
| Ni | atomic | 0.00 | 2.00 | 2.00 | 2.00 | 2.00 | 2.00 |
| | undoped | 0.05 | 1.82 | 1.90 | 1.90 | 1.82 | 1.97 |
| | graphitic | 0.37 | 1.96 | 1.94 | 1.59 | 1.97 | 1.88 |
| | pyridinic | 0.75 | 1.94 | 1.82 | 1.99 | 1.60 | 1.90 |
| Cu | atomic | 1.00 | 2.00 | 2.00 | 2.00 | 2.00 | 2.00 |
| | undoped | 1.00 | 2.00 | 2.00 | 2.00 | 2.00 | 2.00 |
| | graphitic | 1.02 | 2.00 | 1.99 | 1.99 | 2.00 | 1.96 |
| | pyridinic | 1.05 | 1.99 | 1.98 | 2.00 | 1.96 | 1.99 |

form for reference) through natural bonding orbital analysis to better characterize the MSI and the preferential defect adsorption. For Cu, few changes are observed from either N-doped support compared to UC for any of its valence orbitals. Its electron density in each orbital remains unaffected by either defect, with d-orbitals filled, and its s-orbital is half-filled. This very minimal electronic difference corresponds to Cu's overall low adsorption. Moreover, its electronic occupation in UC does not differ at all from its atomic form, presenting that the support itself has a negligible effect.

Fe presented a bias toward $N_GC$ over $N_PC$ in its adsorption and is affected by the support, shown through the change of electronic occupation from its atomic form. There is a greater-than-one-electron increase when Fe moves from UC to $N_PC$ in its s-orbital in which the s-orbital occupation does not change at all from UC to $N_GC$. In Fe with $N_GC$, the total amount of valance electronic occupation remains the same as in Fe with UC. The difference is that the d-orbitals are occupied differently, with the greatest difference being within the $d_{yz}$-orbital, where it goes from being almost unoccupied to half-occupied in going from UC to $N_GC$. With the altered electronic density of $N_GC$, there is perhaps a greater interaction with this specific d-orbital, and the electronic density is reorganized accordingly. With $N_PC$, the total valance electronic occupation increases beyond that of UC and $N_GC$. This aligns with the $V_{MOA}$ as the additional electronic density is from the $sp^2$ orbital of the pyridinic nitrogen to Fe's s-orbital. Comparatively, $N_GC$ electronic rearrangement provides a greater MSI than the extent of charge transfer in $N_PC$.

Co presented a similar bias between $N_GC$ and $N_PC$ as Fe. For Co, deviations between its atomic configuration and UC are relatively small, in agreement with its low $E_{ads}$. With $N_GC$ moving from UC, Co's $d_{xy}$-orbital loses about one electron to its $d_{x^2-y^2}$-orbital. To a much lesser extent, electronic density is transferred from its $d_{yz}$-orbital to its $d_{z^2}$-orbital. There is no change in Co's s-orbitals, thus guided by the d-orbitals' electronic rearrangement. With Co's $CC_{MOA}$, $d_{x^2-y^2}$ has a better orbital overlap with the additional graphitic electrons in the antibonding orbitals than $d_{xy}$ and $d_{yz}$. This larger extent of electronic reorganization may contribute to the greater adsorption seen with $N_GC$ as shown with Fe. Co with $N_PC$ does not present much electronic restructuring or charge transfer with the pyridinic nitrogen. This minimal change matches the much lower adsorption in $N_PC$ when compared to $N_GC$. This bias toward $N_GC$ over $N_PC$ is exacerbated as there is very little indication of interactions between Co and $N_PC$.

Ni does not have this bias for either of the defects, but both defects still have different MSIs with Ni. Ni's atomic occupation is defined by its filled d-orbitals, which is similarly matched when Ni is on UC but with slightly less overall occupation. When examining Ni from UC to $N_GC$, there is a 0.32 electron increase in s-orbital occupancy, whereas in Ni from UC to $N_PC$, the s-orbital occupancy increases by 0.70 electron. The lone pair of $N_PC$ donates into the s-orbital with back bonding through the spatially overlapping $d_{xz}$ and $d_{x^2-y^2}$, shown in Figure S1. This is not the case with $N_GC$ as there again was electron rearrangement but to a much lesser extent than that found with Fe and Co. The greatest change was in Ni's $d_{yz}$ as it lost 0.31 electron from UC to $N_GC$, with the other changes being about 0.10 electron in the other d-orbitals. The s-orbital change is the additional electronic density gained as the total electronic occupation in the d-orbitals between UC and $N_GC$ is about the same. This amount of electronic rearrangement is directive of a lower $N_GC$ MSI that is now comparable to the $N_PC$ MSI. Herein, the electronic structure models predict different MSIs between the two different defects and to different extents in the different periodic Groups.

**3.3. Experimental Investigation of the Effect of Graphitic and Pyridinic Nitrogen Defects on Transition Metal Nucleation.** Given that the downselected metals discussed above are representative of their groups, these same metals are selected for experimental studies. The defect biases elucidated by electronic models were experimentally evaluated through synthesis design and characterization of model NC nanomaterials. Synthesizing NC supports with singular N defects is challenging as most synthesis methods produce NC materials that are heterogeneous in nature, but several studies have determined trends of support properties based on the relative ratio of the N speciations within NCs, which can be introduced through variations in the temperature of pyrolysis.[50,51] In a previous study, we reported the synthesis and detailed characterization of NC nanospheres with varied N content, which were speciation-dependent on the amount of N-precursor and the pyrolysis temperature. In this synthesis, as


https://doi.org/10.1021/acsanm.2c03186
ACS Appl. Nano Mater. 2022, 5, 14922−14933

is typical for many NC syntheses, higher pyrolysis temperatures produce a material with higher graphitic N content with the caveat of an upper-bounded threshold where the material degrades significantly.[47] With the aim of determining trends across the four downselected metals, extreme pyrolysis temperatures (600 and 900 °C) were produced as the N-doped supports for this study. While there are undoubtedly slight differences in morphology and composition of the 600 and 900 °C NC samples, the NC elemental compositions are comparable and consistent across the metals synthesized in this work (see Table S2).

Surface characterization of the two NC supports seen in XPS (Figure 4) demonstrates how, while the chemistry of N in both

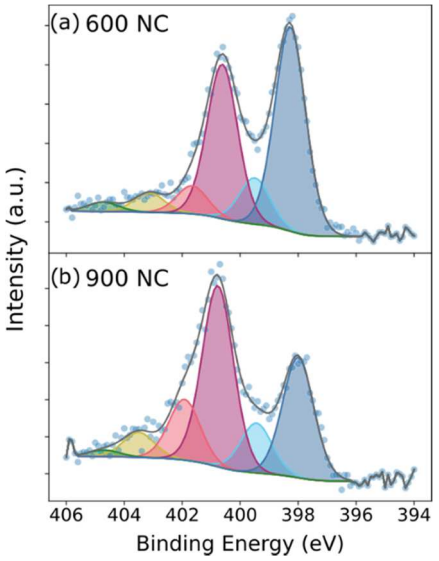


**Figure 4.** High-resolution XPS N 1s spectra of NC materials. NC samples pyrolyzed at (a) 600 °C and (b) 900 °C.

samples is heterogeneous, the two samples have varied N chemical environments. The NC pyrolyzed at 600 °C (Figure 4a) can be described as being rich in pyridinic N species (~398 eV), and the spheres pyrolyzed at 900 °C (Figure 4b) can be described as being rich in graphitic N (~400−402 eV). The 900 °C sample will hereby be referenced as the graphitic-rich NC or $N_G$C-rich, while the 600 °C will be referenced as the pyridinic-rich sample or $N_P$C-rich. Scheme 1 illustrates how these two samples are synthesized and used along with undoped GNPs as supports for Fe, Co, Ni, and Cu. Additional information for XPS fittings can be found in Figure S2.

The incorporation of metals onto the surface of the N-doped nanospheres was conducted using a simple procedure involving a mixture and sonication of the supports with metal salts ($FeCl_2$, $CoCl_2$, $NiCl_2$, and $CuCl_2$). Samples were then pyrolyzed at different temperatures (400, 600, and 800 °C) and analyzed with STEM to determine changes in TM distribution from varying pyrolyzation temperatures. As can be seen for the Ni-NC example in Figure S3, samples pyrolyzed at 400 °C still have a significant Cl signal, as determined by STEM/EDS analysis, meaning the precursor is not decomposed, and the metal signal does not correlate accurately to the nucleated metal content. Samples pyrolyzed at 800 °C resulted in the formation of metal nanoparticles on the NC spheres, and EDS quantification from areas with particles did not accurately represent the extent of nucleation either. This result

**Scheme 1. : Schematic Illustrating the Synthesis Procedure of the Targeted Systems Presented in the Experimental Study**

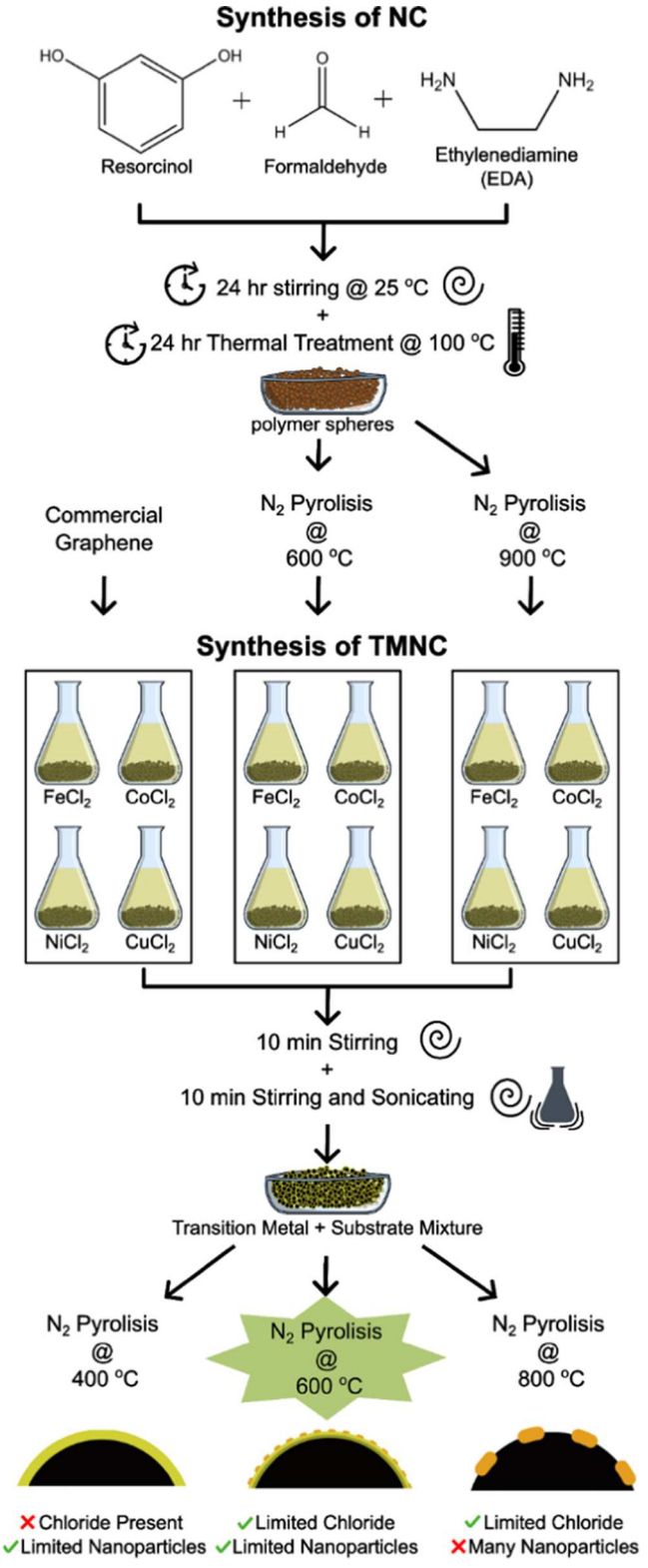


is corroborated by X-ray absorption near edge structure (XANES) spectra of the same Ni-NC sample pyrolyzed at 400, 600, and 800 °C (Figure S4). The 400 °C sample showed a comparable signal to that of the $NiCl_2$ precursor, whereas both the 600 and 800 °C samples had comparable signals to that of


https://doi.org/10.1021/acsanm.2c03186
ACS Appl. Nano Mater. 2022, 5, 14922−14933

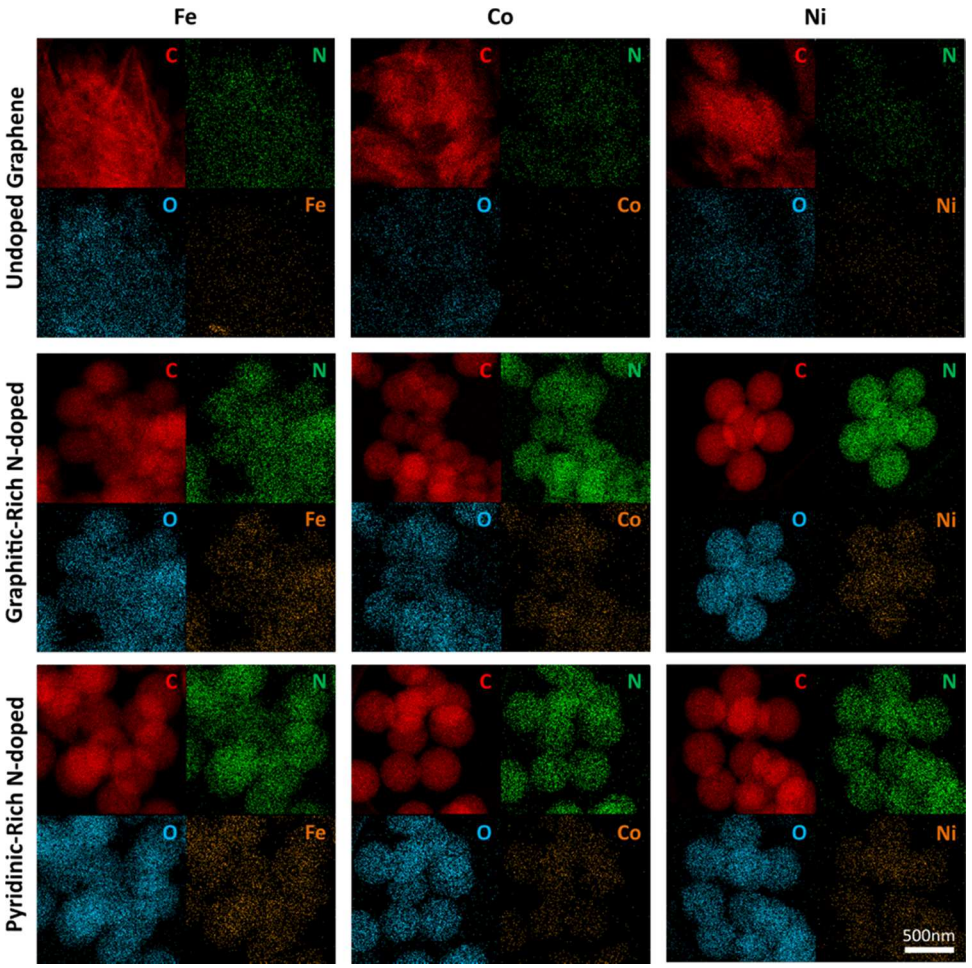


**Figure 5.** STEM/EDS maps that depict the pixels where each element is present within a STEM image. The top row shows each metal sample as deposited on graphene; therefore, very little N and O are present in these samples. C, N, and O are present throughout both N-doped carbon sample sets. All samples were imaged and quantified in locations without large metal nanoparticles, which can be seen by the evenly distributed signal in all metal maps. All images correspond to the same size scale bar seen in the bottom right-hand corner.

the metallic Ni foil reference. Since samples heat-treated at 600 °C demonstrate limited Cl signal from XPS and XANES, as well as very few aggregates of migrated metal, it was determined that this 600 °C heat treatment is most optimal for this study.

In Figure 6, STEM/EDS maps demonstrate the nanoscale elemental distribution of C, N, and O, as well as the respective metal on the selected sample set. Quantified EDS concentrations of C, N, and O across the samples can be seen in Table S2 and are relatively similar for all N-doped samples, although slight variations do exist and may contribute to some of the presented results. STEM/EDS was performed using a low-voltage electron beam of 120 V to ensure a higher likelihood of interaction with smaller atoms and an increase in the number of characteristic X-rays that are collected. C and O maps are presented to visualize where support materials are in each image and demonstrate their homogeneous composition across each nanosphere. A homogeneous distribution of N is seen in all doped NC samples, while the undoped graphene demonstrates a low N signal, which is to be expected. EDS maps of each metal also demonstrate greater signals in the NC nanospheres compared to undoped GNPs. For each sample, metal is evenly distributed on the surface of the supports, without the presence of metal nanoparticles, allowing for direct comparisons of nucleated metal content.

Figure 5 presents the quantification of atomic % metal as determined through the EDS spectra to measure and compare the amount of metal on each sample and, in turn, the affinity of each metal to its support. Each data point shown was taken from areas with a homogeneous distribution of metal, avoiding any areas with metal nanoparticles. Data were acquired from at least five different locations to provide a better representation of each sample.

Greater quantities of all metals are detected on the N-doped supports than on the GNP samples, which consistently demonstrate almost no metal incorporation. While it is noted that the extreme difference in morphology from the graphene to the NC spheres may be partially responsible for the difference in nucleation, it can be assumed that N-doping is a major factor in the increase in nucleation, as has been seen in other reports as well.[7,50] The Fe sample shows a large increase in metal content from the undoped support to the $N_G$C-rich support, demonstrating approximately 1 atomic % of metal incorporation. When Fe is synthesized on the $N_P$C-rich support, it demonstrates a slightly diminished metal content compared to the $N_G$C-rich support, but the metal content is still significantly larger in comparison to the undoped support. Co has the most significant difference between the three supports, with very little Co signal detected in the undoped carbon sample, a higher Co signal measured in the pyridine-


https://doi.org/10.1021/acsanm.2c03186
ACS Appl. Nano Mater. 2022, 5, 14922−14933

rich sample, and the highest Co signal occurring in the graphitic N-rich sample. Ni shows a large increase in metal incorporation for both N defects, with similar values for atomic % of metal on both the graphitic-rich and pyridinic-rich supports. The Cu samples in this study were also synthesized and analyzed, revealing very little to no incorporation of Cu into all three supports, but these samples are not included here due to contamination in the sample related to the impurity of the precursor.

**3.4. Correlations between Experiments and Computations.** While it must be cautioned that the experimental conditions had inevitable deviations from calculated environments, there are some notable correlations seen between the experimental and calculated results. Overall, Figure 6 demonstrates that the $N_GC$-rich supports incorporate the highest amount of metal of all of the substrates in every sample. This atomic percentage correlates with computations that suggested higher MSI with $N_GC$ due to the difference in the mechanism, where the mechanism of $N_GC$ MSI results in increased orbital overlap interactions, while the $N_PC$ MSI mechanism indicates a lone pair interaction. The Ni most likely does not see this discretion as compared to the Fe and Co as its valency is much greater. Additionally, the calculated distinction between $N_PC$ MSI for Fe and Co appears to be supported by their differing atomic percentages in Figure 6. Fe has more metal nucleation on its $N_PC$-rich sample than the corresponding Co sample, which correlates well to the lower adsorption energy that is calculated on the pyridine-rich defect in comparison to Co on the same defect. This could be explained by the greater electronic rearrangement seen in Fe than Co while interacting with a graphitic defect. Ni demonstrated similar affinities of Ni nucleation for both types of N-doped supports, agreeing with the calculated adsorption energy values. The $N_GC$ MSI relies on partially filled orbitals to interact with the graphitic-doped support, which the Ni lacks. Due to this, its $N_PC$ MSI may be able to reach the same degree of strength as the graphitic one, supported experimentally and computationally. It is important to note that there was little integration of Cu metal on these samples (<0.1 atomic %), which was verified by multiple repeated experiments and correlates well to the computational findings in this work, further confirming the limited MSI between Cu and all studied supports. Unfortunately, this sample showed the presence of Ni in all samples, likely due to precursor contamination; therefore, the experimental data obtained for the Cu samples were not included.

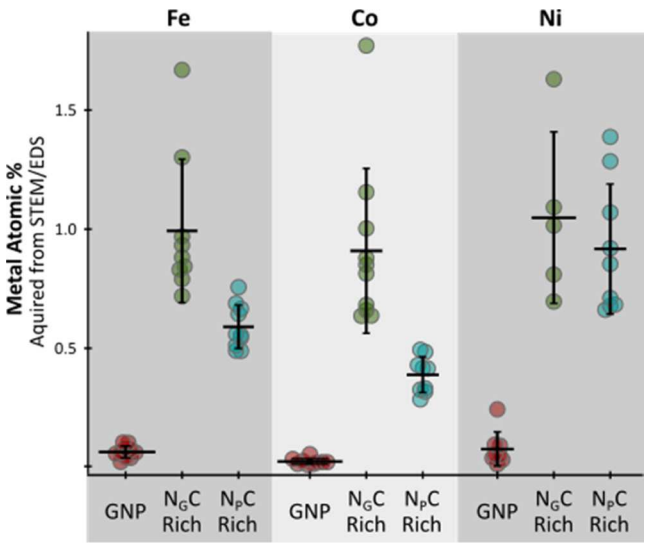


**Figure 6.** Quantification of atomic percent metal in the EDS spectra for each sample. Each point represents quantification from a different image within the same sample. All data were taken from areas with no visible nanoparticles.

Overall, this work demonstrates a broader, more comprehensive investigation of MSI for transition metals on N-doped carbons with correlations between computations and experiments. In general, both types of N defects provide for an increase in the attraction between support and metal, with a bias for graphitic defects supported by the $E_{ads}$ and a larger degree of electronic rearrangement.

## CONCLUSIONS

The study establishes a methodology for exploration of effects of nitrogen doping across different metals and two N defects in carbon-based nanomaterials and shows corroboration of computational data with experimental work supported by established trends for MSI, broadening fundamental knowledge of MSI of the transition metals supported on N-doped carbon. 12 computationally investigated metals were analyzed to determine their $E_{ads}$ and MOA on undoped, graphitic N-doped, and pyridinic N-doped support so that MSI could be described by periodic trends. It was observed that N-doping increased the MSI as shown through calculated $E_{ads}$, but the range of improved $E_{ads}$ varied by these periodic trends. Going from Group 8 to 11, the MSI with graphitic N defect weakened as the valency of the d-orbitals increased such that for Groups 8 and 9, the MSI strength of graphitic N defect was on par with pyridinic's until Group 10, where it was shown to be about the same. Group 11 metals demonstrated almost no interactions with the supports. Given that the MSIs were described by periodic trends, leading group members were narrowed to the experimental studies with the help of computed data. Experimental results were optimized to best compare metal nucleation studies with the presented computational findings. STEM/EDS was used to determine metal affinities toward samples with pyridinic- or graphitic-rich N-doped supports. Further, the nature of the MSI is discussed by comparing these theoretical and experimental findings. Examining the individual electronic influence of the graphitic and pyridinic dopants on the metals, it was seen that while both dopants improved the MSIs, MSIs were affected differently. Fe and Co exhibit a preference for graphitic defect over the pyridinic defect, while Ni appears to be unbiased. Ultimately, it was found that MSI for TM was distinctly improved on both NCs as compared to the undoped graphene. With clear evidence that N-doping enhances MSI, the specific defect type (graphitic and pyridinic) further dictates the overall character of the MSI. The electronic differences between the different TM-NCs were distinguishable, demonstrating the viability of developing a finer tuning of MSI. The calculated adsorption energies and MSI strength correlated well to the experimentally determined metal nucleation/speciation within the samples, confirming the trends seen in computational studies.

While this work only examines the impact of one pyridinic defect available in the carbon support, it should be noted that there are often clusters of pyridinic sites, which impact the interactions with the metal catalysts differently as these interactions largely depend on the size of the vacancy.


https://doi.org/10.1021/acsanm.2c03186
ACS Appl. Nano Mater. 2022, 5, 14922−14933

Furthermore, these vacancies may contain other N-heterocyclic-type dopants, depending on the nitrogen concentration and incorporation method. While such models are omitted from this study, it is an interesting area for future studies. By addressing the underlying fundamental nature of the MSI and showcasing two layers of tunability through defect type and supported TM, these findings present imperative contributions to the comprehension and advancement of deliberately designed nanoscale catalyst−support systems through N-doping. The information presented in this work could be utilized in the further development of catalysts in various catalytic applications. Moreover, the methodology presented here can be used for similar comprehensive MSI studies of other systems.

## ■ ASSOCIATED CONTENT

### Supporting Information

The Supporting Information is available free of charge at https://pubs.acs.org/doi/10.1021/acsanm.2c03186.

Additional adsorption data; visual representation of the HOMO levels for the downselected metals over the studied supports; and further characterization through XPS, STEM, and XANES (PDF)

## ■ AUTHOR INFORMATION


### Corresponding Authors

**Shubham Vyas** − *Department of Chemistry, Colorado School of Mines, Golden, Colorado 80401, United States;* orcid.org/0000-0002-5849-8919; Email: svyas@mines.edu

**Svitlana Pylypenko** − *Department of Chemistry, Colorado School of Mines, Golden, Colorado 80401, United States;* orcid.org/0000-0001-7982-734X; Email: spylypen@mines.edu

### Authors

**Vu T. Nguyen** − *Department of Chemistry, Colorado School of Mines, Golden, Colorado 80401, United States;* orcid.org/0000-0002-4363-9803

**Margaret A. Fitzgerald** − *Department of Chemistry, Colorado School of Mines, Golden, Colorado 80401, United States;* orcid.org/0000-0003-2976-0145

**Denali Ibbotson** − *Department of Chemistry, Colorado School of Mines, Golden, Colorado 80401, United States*

**Jayson Foster** − *Department of Chemistry, Colorado School of Mines, Golden, Colorado 80401, United States*

**Michael J. Dzara** − *Department of Chemistry, Colorado School of Mines, Golden, Colorado 80401, United States;* orcid.org/0000-0001-8125-0586

**Sarah F. Zaccarine** − *Department of Chemistry, Colorado School of Mines, Golden, Colorado 80401, United States;* orcid.org/0000-0002-7978-915X

Complete contact information is available at: https://pubs.acs.org/10.1021/acsanm.2c03186


### Notes

The authors declare no competing financial interest.

## ■ ACKNOWLEDGMENTS

This work was funded by the National Science Foundation (CHE-1800585). The authors acknowledge the computational resources allocated by the high-performance computing facility at the Colorado School of Mines (Mines). The authors also acknowledge Mines' Shared Instrumentation Facility, specifically the microscopy resources, and use of the E-XPS system at Mines, which was supported by the National Science Foundation under Grant No. 1626619. The authors would like to thank Dr. David Diercks for assistance with electron microscopy analysis XAS and useful discussions.

## ■ REFERENCES


(1) Yang, X. F.; Wang, A.; Qiao, B.; Li, J.; Liu, J.; Zhang, T. Single-Atom Catalysts: A New Frontier in Heterogeneous Catalysis. *Acc. Chem. Res.* **2013**, *46*, 1740−1748.

(2) Chen, Y.; Ji, S.; Chen, C.; Peng, Q.; Wang, D.; Li, Y. Single-Atom Catalysts: Synthetic Strategies and Electrochemical Applications. *Joule* **2018**, *2*, 1242−1264.

(3) Antolini, E.; Salgado, J. R. C.; Gonzalez, E. R. The Stability of Pt-M (M = First Row Transition Metal) Alloy Catalysts and Its Effect on the Activity in Low Temperature Fuel Cells. A Literature Review and Tests on a Pt-Co Catalyst. *J. Power Sources* **2006**, *160*, 957−968.

(4) Pylypenko, S.; Borisevich, A.; More, K. L.; Corpuz, A. R.; Holme, T.; Dameron, A. A.; Olson, T. S.; Dinh, H. N.; Gennett, T.; O'Hayre, R. Nitrogen: Unraveling the Secret to Stable Carbon-Supported Pt-Alloy Electrocatalysts. *Energy Environ. Sci.* **2013**, *6*, 2957−2964.

(5) Gerber, I. C.; Serp, P. A Theory/Experience Description of Support Effects in Carbon-Supported Catalysts. *Chem. Rev.* **2020**, *120*, 1250−1349.

(6) Shao, Y.; Dodelet, J. P.; Wu, G.; Zelenay, P. PGM-Free Cathode Catalysts for PEM Fuel Cells: A Mini-Review on Stability Challenges. *Adv. Mater.* **2019**, *31*, No. 1807615.

(7) Wood, K. N.; O'Hayre, R.; Pylypenko, S. Recent Progress on Nitrogen/Carbon Structures Designed for Use in Energy and Sustainability Applications. *Energy Environ. Sci.* **2014**, *7*, 1212−1249.

(8) Zhou, Y.; Neyerlin, K.; Olson, T. S.; Pylypenko, S.; Bult, J.; Dinh, H. N.; Gennett, T.; Shao, Z.; O'Hayre, R. Enhancement of Pt and Pt-Alloy Fuel Cell Catalyst Activity and Durability via Nitrogen-Modified Carbon Supports. *Energy Environ. Sci.* **2010**, *3*, 1437−1446.

(9) Tang, H.; Chen, J. H.; Huang, Z. P.; Wang, D. Z.; Ren, Z. F.; Nie, L. H.; Kuang, Y. F.; Yao, S. Z. High Dispersion and Electrocatalytic Properties of Platinum on Well-Aligned Carbon Nanotube Arrays. *Carbon* **2004**, *42*, 191−197.

(10) Xu, J. B.; Zhao, T. S. Mesoporous Carbon with Uniquely Combined Electrochemical and Mass Transport Characteristics for Polymer Electrolyte Membrane Fuel Cells. *RSC Adv.* **2013**, *3*, 16−24.

(11) Holme, T.; Zhou, Y.; Pasquarelli, R.; O'Hayre, R. First Principles Study of Doped Carbon Supports for Enhanced Platinum Catalysts. *Phys. Chem. Chem. Phys.* **2010**, *12*, 9461−9468.

(12) Xue, D.; Xia, H.; Yan, W.; Zhang, J.; Mu, S. Defect Engineering on Carbon-Based Catalysts for Electrocatalytic CO2 Reduction. *Nano-Micro Lett.* **2020**, *13*, No. 5.

(13) Wood, K. N.; O'Hayre, R.; Pylypenko, S. Recent Progress on Nitrogen/Carbon Structures Designed for Use in Energy and Sustainability Applications. *Energy Environ. Sci.* **2014**, *7*, 1212−1249.

(14) Zhou, Y.; Neyerlin, K.; Olson, T. S.; Pylypenko, S.; Bult, J.; Dinh, H. N.; Gennett, T.; Shao, Z.; O'Hayre, R. Enhancement of Pt and Pt-Alloy Fuel Cell Catalyst Activity and Durability via Nitrogen-Modified Carbon Supports. *Energy Environ. Sci.* **2010**, *3*, 1437−1446.

(15) Qu, L.; Liu, Y.; Baek, J. B.; Dai, L. Nitrogen-Doped Graphene as Efficient Metal-Free Electrocatalyst for Oxygen Reduction in Fuel Cells. *ACS Nano* **2010**, *4*, 1321−1326.

(16) Paraknowitsch, J. P.; Thomas, A. Doping Carbons beyond Nitrogen: An Overview of Advanced Heteroatom Doped Carbons with Boron, Sulphur and Phosphorus for Energy Applications. *Energy Environ. Sci.* **2013**, *6*, 2839−2855.

(17) Perazzolo, V.; Brandiele, R.; Durante, C.; Zerbetto, M.; Causin, V.; Rizzi, G. A.; Cerri, I.; Granozzi, G.; Gennaro, A. Density Functional Theory (DFT) and Experimental Evidences of Metal-Support Interaction in Platinum Nanoparticles Supported on

Nitrogen- and Sulfur-Doped Mesoporous Carbons: Synthesis, Activity, and Stability. *ACS Catal.* **2018**, *8*, 1122−1137.
(18) Quílez-Bermejo, J.; Morallón, E.; Cazorla-Amorós, D. Metal-Free Heteroatom-Doped Carbon-Based Catalysts for ORR. A Critical Assessment about the Role of Heteroatoms. *Carbon* **2020**, *165*, 434−454.
(19) Wu, Z.; Song, M.; Wang, J.; Liu, X. Recent Progress in Nitrogen-Doped Metal-Free Electrocatalysts for Oxygen Reduction Reaction. *Catalysts* **2018**, *8*, No. 196.
(20) Guo, J.; Huo, J.; Liu, Y.; Wu, W.; Wang, Y.; Wu, M.; Liu, H.; Wang, G. Nitrogen-Doped Porous Carbon Supported Nonprecious Metal Single-Atom Electrocatalysts: From Synthesis to Application. *Small Methods* **2019**, *3*, No. 1900159.
(21) Arrigo, R.; Schuster, M. E.; Xie, Z.; Yi, Y.; Wowsnick, G.; Sun, L. L.; Hermann, K. E.; Friedrich, M.; Kast, P.; Hävecker, M.; Knop-Gericke, A.; Schlögl, R. Nature of the N-Pd Interaction in Nitrogen-Doped Carbon Nanotube Catalysts. *ACS Catal.* **2015**, *5*, 2740−2753.
(22) Sun, C. L.; Chen, L. C.; Su, M. C.; Hong, L. S.; Chyan, O.; Hsu, C. Y.; Chen, K. H.; Chang, T. F.; Chang, L. Ultrafine Platinum Nanoparticles Uniformly Dispersed on Arrayed CNx Nanotubes with High Electrochemical Activity. *Chem. Mater.* **2005**, *17*, 3749−3753.
(23) Wang, X.; Sun, G.; Routh, P.; Kim, D. H.; Huang, W.; Chen, P. Heteroatom-Doped Graphene Materials: Syntheses, Properties and Applications. *Chem. Soc. Rev.* **2014**, *43*, 7067−7098.
(24) Muhich, C. L.; Westcott, J. Y.; Morris, T. C.; Weimer, A. W.; Musgrave, C. B. The Effect of N and B Doping on Graphene and the Adsorption and Migration Behavior of Pt Atoms. *J. Phys. Chem. C* **2013**, *117*, 10523−10535.
(25) Corpuz, A. R.; Olson, T. S.; Joghee, P.; Pylypenko, S.; Dameron, A. A.; Dinh, H. N.; O'Neill, K. J.; Hurst, K. E.; Bender, G.; Gennett, T.; Pivovar, B. S.; Richards, R. M.; O'Hayre, R. P. Effect of a Nitrogen-Doped PtRu/Carbon Anode Catalyst on the Durability of a Direct Methanol Fuel Cell. *J. Power Sources* **2012**, *217*, 142−151.
(26) Zhou, Y.; Holme, T.; Berry, J.; Ohno, T. R.; Ginley, D.; O'Hayre, R. Dopant-Induced Electronic Structure Modification of HOPG Surfaces: Implications for High Activity Fuel Cell Catalysts. *J. Phys. Chem. C* **2010**, *114*, 506−515.
(27) Bulushev, D. A.; Zacharska, M.; Shlyakhova, E. V.; Chuvilin, A. L.; Guo, Y.; Beloshapkin, S.; Okotrub, A. V.; Bulusheva, L. G. Single Isolated Pd2+ Cations Supported on N-Doped Carbon as Active Sites for Hydrogen Production from Formic Acid Decomposition. *ACS Catal.* **2016**, *6*, 681−691.
(28) Zhao, W.; Zhang, L.; Luo, Q.; Hu, Z.; Zhang, W.; Smith, S.; Yang, J. Single Mo1(Cr1) Atom on Nitrogen-Doped Graphene Enables Highly Selective Electroreduction of Nitrogen into Ammonia. *ACS Catal.* **2019**, *9*, 3419−3425.
(29) Zhang, S.; Wang, H.; Zhang, N.; Kong, F.; Liu, H.; Yin, G. Role of Pt-Pyridinic Nitrogen Sites in Methanol Oxidation on Pt/Polypyrrole-Carbon Black Catalyst. *J. Power Sources* **2012**, *197*, 44−49.
(30) Zhou, Y.; Neyerlin, K.; Olson, T. S.; Pylypenko, S.; Bult, J.; Dinh, H. N.; Gennett, T.; Shao, Z.; O'Hayre, R. Enhancement of Pt and Pt-Alloy Fuel Cell Catalyst Activity and Durability via Nitrogen-Modified Carbon Supports. *Energy Environ. Sci.* **2010**, *3*, 1437−1446.
(31) Ye, S.; Vijh, A. K.; Dao, L. H. A New Fuel Cell Electrocatalyst Based on Carbonized Polyacrylonitrile Foam: The Nature of Platinum-Support Interactions. *J. Electrochem. Soc.* **1997**, *144*, 90−95.
(32) Yang, M.; Wang, L.; Li, M.; Hou, T.; Li, Y. Structural Stability and O2 Dissociation on Nitrogen-Doped Graphene with Transition Metal Atoms Embedded: A First-Principles Study. *AIP Adv.* **2015**, *5*, No. 067136.
(33) Kaiser, S. K.; Chen, Z.; Faust Akl, D.; Mitchell, S.; Pérez-Ramírez, J. Single-Atom Catalysts across the Periodic Table. *Chem. Rev.* **2020**, *120*, 11703−11809.
(34) Yang, H.; Wu, Y.; Li, G.; Lin, Q.; Hu, Q.; Zhang, Q.; Liu, J.; He, C. Scalable Production of Efficient Single-Atom Copper Decorated Carbon Membranes for CO2 Electroreduction to Methanol. *J. Am. Chem. Soc.* **2019**, *141*, 12717−12723.
(35) Marshall-Roth, T.; Libretto, N. J.; Wrobel, A. T.; Anderton, K. J.; Pegis, M. L.; Ricke, N. D.; Voorhis, T.; Van; Miller, J. T.; Surendranath, Y. A Pyridinic Fe-N4 Macrocycle Models the Active Sites in Fe/N-Doped Carbon Electrocatalysts. *Nat. Commun.* **2020**, *11*, No. 5283.
(36) Zitolo, A.; Ranjbar-Sahraie, N.; Mineva, T.; Li, J.; Jia, Q.; Stamatin, S.; Harrington, G. F.; Lyth, S. M.; Krtil, P.; Mukerjee, S.; Fonda, E.; Jaouen, F. Identification of Catalytic Sites in Cobalt-Nitrogen-Carbon Materials for the Oxygen Reduction Reaction. *Nat. Commun.* **2017**, *8*, No. 957.
(37) Hossain, M. D.; Liu, Z.; Zhuang, M.; Yan, X.; Xu, G. L.; Gadre, C. A.; Tyagi, A.; Abidi, I. H.; Sun, C. J.; Wong, H.; Guda, A.; Hao, Y.; Pan, X.; Amine, K.; Luo, Z. Rational Design of Graphene-Supported Single Atom Catalysts for Hydrogen Evolution Reaction. *Adv. Energy Mater.* **2019**, *9*, No. 1803689.
(38) Calle-Vallejo, F.; Martínez, J. I.; Rossmeisl, J. Density Functional Studies of Functionalized Graphitic Materials with Late Transition Metals for Oxygen Reduction Reactions. *Phys. Chem. Chem. Phys.* **2011**, *13*, 15639−15643.
(39) Jiang, W. J.; Gu, L.; Li, L.; Zhang, Y.; Zhang, X.; Zhang, L. J.; Wang, J. Q.; Hu, J. S.; Wei, Z.; Wan, L. J. Understanding the High Activity of Fe-N-C Electrocatalysts in Oxygen Reduction: Fe/Fe3C Nanoparticles Boost the Activity of Fe-Nx. *J. Am. Chem. Soc.* **2016**, *138*, 3570−3578.
(40) Zhang, H.; Hwang, S.; Wang, M.; Feng, Z.; Karakalos, S.; Luo, L.; Qiao, Z.; Xie, X.; Wang, C.; Su, D.; Shao, Y.; Wu, G. Single Atomic Iron Catalysts for Oxygen Reduction in Acidic Media: Particle Size Control and Thermal Activation. *J. Am. Chem. Soc.* **2017**, *139*, 14143−14149.
(41) Wang, Q.; Ina, T.; Chen, W. T.; Shang, L.; Sun, F.; Wei, S.; Sun-Waterhouse, D.; Telfer, S. G.; Zhang, T.; Waterhouse, G. I. N. Evolution of Zn(II) Single Atom Catalyst Sites during the Pyrolysis-Induced Transformation of ZIF-8 to N-Doped Carbons. *Sci. Bull.* **2020**, *65*, 1743−1751.
(42) Chen, Y.; Ji, S.; Chen, C.; Peng, Q.; Wang, D.; Li, Y. Single-Atom Catalysts: Synthetic Strategies and Electrochemical Applications. *Joule* **2018**, *2*, 1242−1264.
(43) Groves, M. N.; Chan, A. S. W.; Malardier-Jugroot, C.; Jugroot, M. Improving Platinum Catalyst Binding Energy to Graphene through Nitrogen Doping. *Chem. Phys. Lett.* **2009**, *481*, 214−219.
(44) Nguyen, V.; Etz, B. D.; Pylypenko, S.; Vyas, S. Periodic Trends behind the Stability of Metal Catalysts Supported on Graphene with Graphitic Nitrogen Defects. *ACS Omega* **2021**, *6*, 28215−28228.
(45) Frisch, M. J.; Trucks, G. W.; Schlegel, H. B.; Scuseria, G. E.; Robb, M. A.; Cheeseman, J. R.; Scalmani, G.; Barone, V.; Petersson, G. A.; Nakatsuji, H.; Li, X.; Caricato, M.; Marenich, A. V.; Bloino, J.; Janesko, B. G.; Gomperts, R.; Mennucci, B.; Hratchian, H. P.; V, J.; J F, D. *Gaussian 16*; Gaussian, Inc.: Wallingford CT, 2016.
(46) Wickramaratne, N. P.; Xu, J.; Wang, M.; Zhu, L.; Dai, L.; Jaroniec, M. Nitrogen Enriched Porous Carbon Spheres: Attractive Materials for Supercapacitor Electrodes and CO2 Adsorption. *Chem. Mater.* **2014**, *26*, 2820−2828.
(47) Ngo, C.; Fitzgerald, M. A.; Dzara, M. J.; Strand, M. B.; Diercks, D. R.; Pylypenko, S. 3D Atomic Understanding of Functionalized Carbon Nanostructures for Energy Applications. *ACS Appl. Nano Mater.* **2020**, *3*, 1600−1611.
(48) van Deelen, T. W.; Hernández Mejía, C.; de Jong, K. P. Control of Metal-Support Interactions in Heterogeneous Catalysts to Enhance Activity and Selectivity. *Nat. Catal.* **2019**, *2*, 955−970.
(49) Lou, Y.; Xu, J.; Zhang, Y.; Pan, C.; Dong, Y.; Zhu, Y. Metal-Support Interaction for Heterogeneous Catalysis: From Nanoparticles to Single Atoms. *Mater. Today Nano* **2020**, *12*, No. 100093.
(50) Pylypenko, S.; Queen, A.; Olson, T. S.; Dameron, A.; Oneill, K.; Neyerlin, K. C.; Pivovar, B.; Dinh, H. N.; Ginley, D. S.; Gennett, T.; Ohayre, R. Tuning Carbon-Based Fuel Cell Catalyst Support Structures via Nitrogen Functionalization. II. Investigation of Durability of Pt-Ru Nanoparticles Supported on Highly Oriented Pyrolytic Graphite Model Catalyst Supports as a Function of Nitrogen Implantation Dose. *J. Phys. Chem. C* **2011**, *115*, 13676−13684.


https://doi.org/10.1021/acsanm.2c03186
*ACS Appl. Nano Mater.* 2022, 5, 14922−14933

(51) Higgins, D. C.; Meza, D.; Chen, Z. Nitrogen-Doped Carbon Nanotubes as Platinum Catalyst Supports for Oxygen Reduction Reaction in Proton Exchange Membrane Fuel Cells. *J. Phys. Chem. C* **2010**, *114*, 21982−21988.





https://doi.org/10.1021/acsanm.2c03186
*ACS Appl. Nano Mater.* 2022, 5, 14922−14933